Supporting Information

Macroscopic Versus Microscopic Schottky Barrier determination at (Au/Pt)/Ge (100): Interfacial Local Modulation

Andrea Gerbi,[*],[†] Renato Buzio,[†] Cesar González,[‡] Nicola Manca,[†],[#] Daniele Marrè,[†],[#] Sergio Marras,[¶] Mirko Prato,[¶] Lloyd Bell,[§] Sergio Di Matteo,[‖] Fernando Flores,[‡] and Pedro L. de Andres[⊥]

†CNR-SPIN, C.so Perrone 24, I-16152 Genova, Italy

‡Física Teórica de la Materia Condensada-IFIMAC, Universidad Autonoma de Madrid, E-28049 Madrid, Spain

¶Materials Characterization Facility, Istituto Italiano di Tecnologia, Via Morego 30, I-16163 Genova, Italy

§Jet Propulsion Laboratory, California Institute of Technology, 4800 Oak Grove Dr. Pasadena, CA 91104, USA

‖Univ. Rennes, CNRS, IPR (Institut de Physique de Rennes) - UMR 6251, F-35000 Rennes, France

⊥Instituto de Ciencia de Materiales de Madrid-CSIC, Cantoblanco, E-28049 Madrid, Spain

#Dipartimento di Fisica, Universita degli Studi di Genova, via Dodecaneso 33, 16146 Genova, Italy

E-mail: andrea.gerbi@spin.cnr.it

S1   X-ray Photoelectron Spectroscopy (XPS)

The XPS analyses were carried out with a Kratos Axis Ultra[DLD] spectrometer using a monochromatic Al K(α) source operated at 20 mA and 15 kV. Wide scan analysis were carried out with an analysis area of 300×700 microns and a pass energy of 160 eV. High-resolution spectra were acquired with the same analysis area and a pass energy of 10 eV. Spectra have been charge-corrected to the main line of the carbon 1s spectrum (adventitious carbon) set to 284.8 eV. Spectra were analysed using CasaXPS software (version 2.3.19).

Please note that the analyses could not be performed immediately after the wet etching process but only after approximatelu one hour, during which the samples were kept in rough vacuum after being exposed to air for a few minutes.
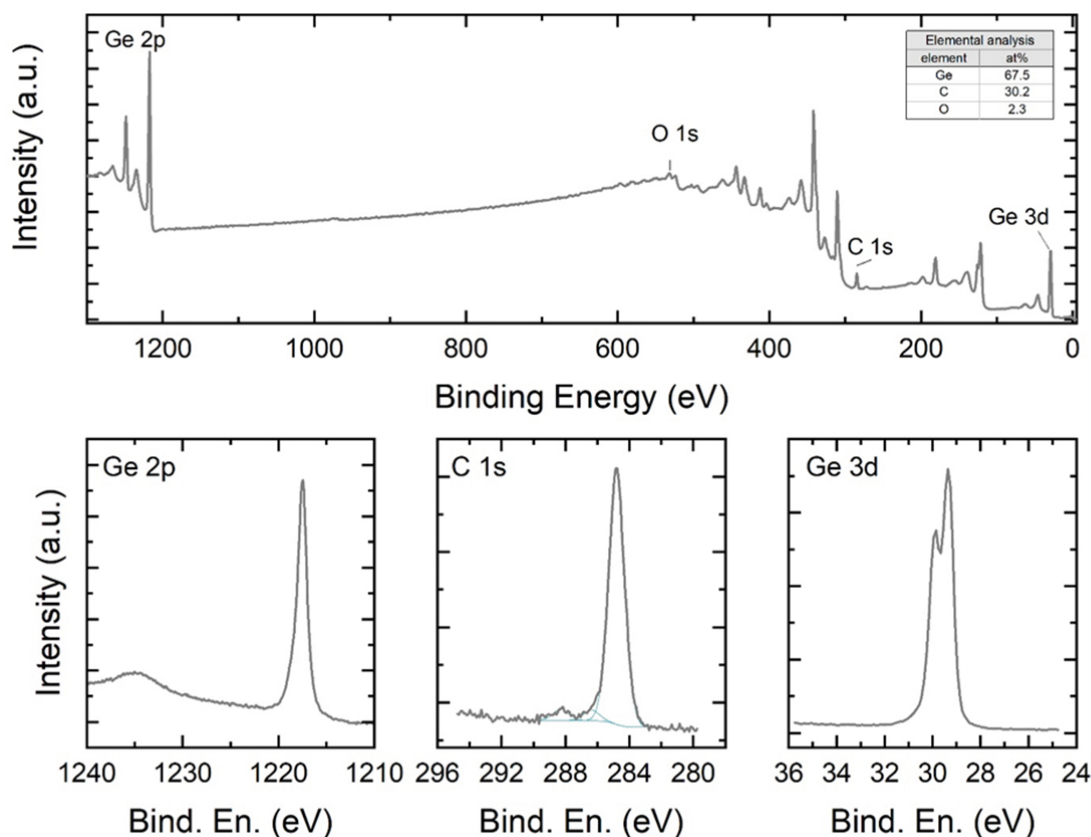
Figure S1: Top panel shows a typical XPS wide scan. Bottom panel shows the Binding Energy for the levels Ge 2p (left), C 1s (center) and Ge 3d (right) respectively.

The XPS data collected on such a representative sample are shown in Figure S1.

The top panel shows a typical wide scan, in which all the peaks could be assigned to specific Ge transitions (both XPS and Auger peaks, see ref.[1] for a comparison) apart from the peak at approx. 285 eV, due to carbon. At approx. 530 eV, a low-intensity O 1s peak could also be observed. By calculating the area under the main peaks for each element, and dividing it by the so-called *relative sensitivity factors*, we extracted the composition of the surface of the sample (results are reported in the inset of the top panel). Please note that precise quantification of the oxygen content is however tricky, due to the overlap with Ge Auger LMM features in the same energy range. Therefore, the reported oxygen content value has to be considered as an upper limit.

Carbon content appears to be quite high, which is not a surprise since it is known that a layer of carbonaceous material is usually found on the surface of most air-exposed samples. Importantly, this adventitious carbon layer is usually reported to be a series of well dispersed, rather uniform, nanostructures physisorbed onto the sample and not chemically involved with the original surface species.[2] From a chemical point of view, this carbonaceous layer predominantly consists of hydrocarbon species (C-C/C-H, main peak at 284.8 eV in bottom center panel), together with minor components (less than 10% of the total signal intensity) due to carbo-oxides containing C-O-C (peak at 286.4 eV) and O-C=O (peak at 288.3 eV) bonds, in agreement with literature reports.[3]

To give an estimate of the thickness of this carbonaceous layer, we performed short Ar^+ ion sputtering cycles (kinetic energy = 500 eV) to expose the clean, uncoated Ge surface. Most of the carbon signal ($\approx 80\%$) was removed after 5 s of sputtering. Longer exposures to the ion beam resulted in a relevant amorphization of Ge (visible as broadening of the Ge 3d peaks) and were therefore avoided.

From the change in intensity of the Ge 3d peaks with the ion etching, we evaluated the effective thickness of the removed carbonaceous layer, using a Beer-Lambert relation $I = I_0 e^{-\frac{d}{\lambda}}$ where I is the measured intensity of the Ge 3d peak before sputtering, I_0 is its

intensity after the removal of the carbonaceous layer, d is the thickness of the carbonaceous layer and λ is the electron attenuation length, that for Ge 3d electrons through an organic layer is approximately 3 nm.

The increase of intensity of Ge 3d observed after Ar^+ sputtering corresponds to a carbonaceous layer thickness of approximately 0.5 nm.

As said before, the presence of this layer is likely to be due to exposure of the sample to air after the wet etching process and, as reported in literature, its thickness/coverage is strictly related to the exposure time. Therefore, the thickness we have estimated here is larger than the typical one (see below further discussion on this aspect).

We then analyzed more in detail the Ge signals, looking for surface oxidations and/or chemical involvement of Ge with species that could come from the wet etching process itself. Bottom left and bottom right panels in Figure S1 show signals collected over the binding energy ranges typical for Ge $2p_{\frac{3}{2}}$ and Ge 3d peaks, respectively.

Ge $2p_{\frac{3}{2}}$ range is characterized by the presence of a single peak centered at 1217.5 eV, in good agreement with reports on Ge(0).[4] At the same time, we can also say that there are no clear indications for the presence of GeO_2 or GeF_2 species, which should result in XPS peaks at higher binding energy values (around 1220.6 eV, same ref.).

Similar information could be obtained by analyzing the Ge 3d doublet. Our data show the presence of a well resolved doublet with the main component Ge $3d_{\frac{5}{2}}$ centered at 29.3 eV, in agreement with what has been reported for Ge(0).[4] GeO_2 species typically contribute to the spectrum with signals at approx. 32.5 eV, not present on our sample.

Together, analysis of the Ge peaks suggests that the wet etching process did not form oxide or fluoride species at the surface of the germanium substrate. Following the example of,[5] we have also performed a deeper analysis of the Ge 3d profile. The results are shown in Figure S2.

Here, two doublets were used to obtain the best fit to the data; the most intense one, accounting for approximately 95% of the total Ge, is attributed to elemental Ge - Ge(0),
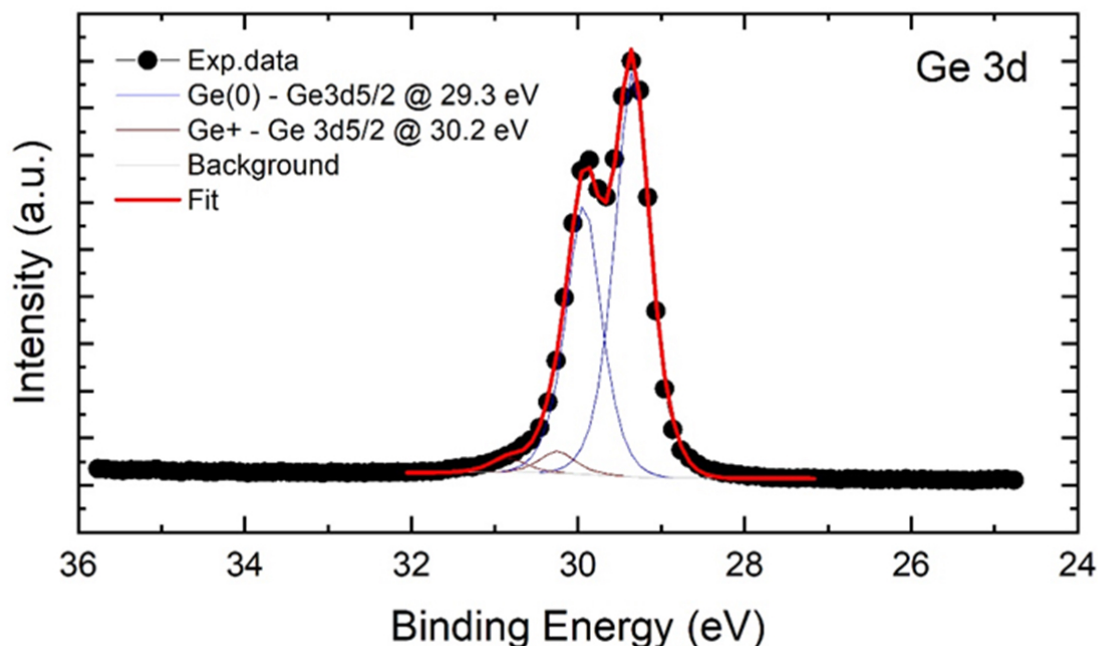
Figure S2: Peak fitting of Ge 3d showing a doublet with the main component Ge 3d$_{\frac{5}{2}}$ centered at 29.3 eV, together with a low intensity doublet at higher binding energy, that could account for surface Ge atoms, terminated by OH^- groups.

and the other, in analogy to what has been discussed in the reference cited above, it is most likely due to Ge surface atoms, terminated by OH^- group. We calculated the hydroxide coverage, obtaining a value of 0.2 ML.

Concerning the C and O surface contamination, several papers in the literature report how the HF treatment can passivate well the Germanium surface inducing a strong reduction of the reoxidation (due to the H termination of the surface). However, passivation is not enough to prevent carbon contamination. In the paper by Rivillon et al.,,[6] the authors demonstrated that, after the HF etching, signals from O 1s level disappear. They showed the presence of carbon contamination due to air exposure, also reported by Terri Deegan et al.,[7] where the authors claim that the carbon contamination originates from a combination of adventitious carbon and hydrocarbons physisorbed onto the sample surface during its exposure to ambient conditions. This behaviour is similar to that observed on silicon, for which hydrophobic H-terminated surfaces attract more hydrocarbons contamination than

hydrophilic oxide. For this reason, the duration of the ambient exposure is very important. For device fabrication, we typically introduced the sample in the HV chamber in a time $le5$ min (10^{-6} mbar), but for XPS measurements the exposition time was significantly longer (one hour) although the samples were transferred under low vacuum conditions (10^{-2} mbar). The reactivity toward the reoxidation is considerably slower. Other groups[8] also reported that the rate of oxidation is slower when the Ge surface was treated in more diluted HF. In other words, the Ge surface can stay stable in air for a longer time when the surface was treated in a more diluted HF and had an atomically smoother surface. Therefore, the treatment of the Ge surface in a highly diluted HF has an advantage in the surface preparation, suppressing oxidation of Ge in air ambient. These considerations suggest that most of the contamination comes from the exposure time of the sample to the ambient conditions.

To further corroborate our claims, it is also known that the presence of a thin oxygen layer strongly reduce the Schottky Barrier due to the depinning effect of the Fermi level.[9] In our case the Schottky barrier measured by macroscopic current voltage characterization (thermionic model) and by BEEM measurements are in excellent agreement with the data reported in literature indicating that at the interface oxygen contamination is not significant. In addition, the distribution of the barriers measured by BEEM is very narrow (less than 20 meV) and centered around the optimal value, highlighting that on the spatial scale probed by this technique (up to 1μm $\times$ 1μm) the contaminations are negligible. In fact, we do not observe important fluctuations neither in the value of the barrier nor in the values of the transmittance (thin carbon layers at the interface generally produce strong reduction in the ballistic signal due to backscattering processes).

Furthermore, as evidenced by the BEEM data, the transmittance of our interface (I_B/I_T of order of a few percent at 1 V) is very similar to that reported for interfaces prepared under UHV with a clean interface, e.g. BiSi(100)[10] or Ag/Si(100)[11]) and for Au/Si(100)[12] prepared by wet chemical etching. These elements suggest that the interface contamination is negligible on the spatial scale investigated by BEEM.

Finally, we have also prepared Schottky junctions between evaporated Au on Ar$^+$ sputtered and annealed Ge(100) (E = 1 KeV, I = 8×10^{-6} A of Argon ions for 35 min at P(Ar) = 3×10^{-5} mbar, 60° angle of incident with respect to the normal to the sample, sputtering time t = 2100 s). We have repeated the procedure three times. The annealing temperature was 800 C. We have measured by BEEM the same value of the barrier obtained after the wet chemical etching. On the contrary, concluding the surface preparation with the sputtering as last step (without annealing) we have observed a reduction of the barrier to 0.5 eV (data not showed).

S2   Structural characterization by XRD: technical details

X-ray Diffraction (XRD) patterns were recorded on a Rigaku SmartLab X-ray powder diffractometer equipped with a 9 kW Cu Kα rotating anode and five axis goniometer, operating at 40 kV and 150 mA. A Göbel mirror was used to convert the divergent X-ray beam into a parallel beam and to suppress the Cu Kβ radiation.

In plane measurements: IS (incident slit): 0.1mm RS1 e RS2 (receiver slit): 20mm, PSC (parallel slit collimator): 0.5°, PSA (parallel slit analyzer): 0.5deg, Omega (incident beam): 0.4°. *Out of plane measurements*: IS, RS1, RS2: 1mm, Soller: 5.0°.

S2.1   Au/Ge(100) thin films grown by PLD and PVD

A typical out of plane X-ray diffraction pattern of a Au thin film grown by PLD onto Ge(100) (nominal thickness 35 nm) is shown in Figure S3 (note that PVD thin films exhibit the same type of XRD pattern). The pattern shows a very intense peak, associated with the Ge reflection (400) (2θ = 66.3°), preceded by two parasitic lines (CuKβ at 58.9° and WLα1 at 62.9°) characteristics for the copper X-ray tube. The Au thin film shows only one peak, associated to the (220) family of lattice planes (2θ = 64.5°). This indicates a strong preferential orientation of the crystalline domains along the [110] crystallographic direction.

The analysis of the rocking curves (Figure S4) reveals a full-width-at-half-maximum FWHM of 1.207° for Au(220), which is considerably higher than that of the Ge(400) substrate (FWHM=0.035°). The rocking curve allows to obtain information on the angular dispersion of the Au crystalline domains along the [110] direction.

Analysis of the ϕ-scans in turn provides information on the in-plane epitaxy, since any set of lattice planes perpendicular to the surface can be brought into diffraction. The XRD ϕ-scans patterns of the Au film show twice the number of peaks expected assuming merely an epitaxial growth along the [110] direction (Figure S5). This means that the Au thin film consists of two different types of epitaxy textures for the Au(110)/Ge(100) system, rotated by 90° one with respect to the other. Indeed, the crystallographic orientation along the direction
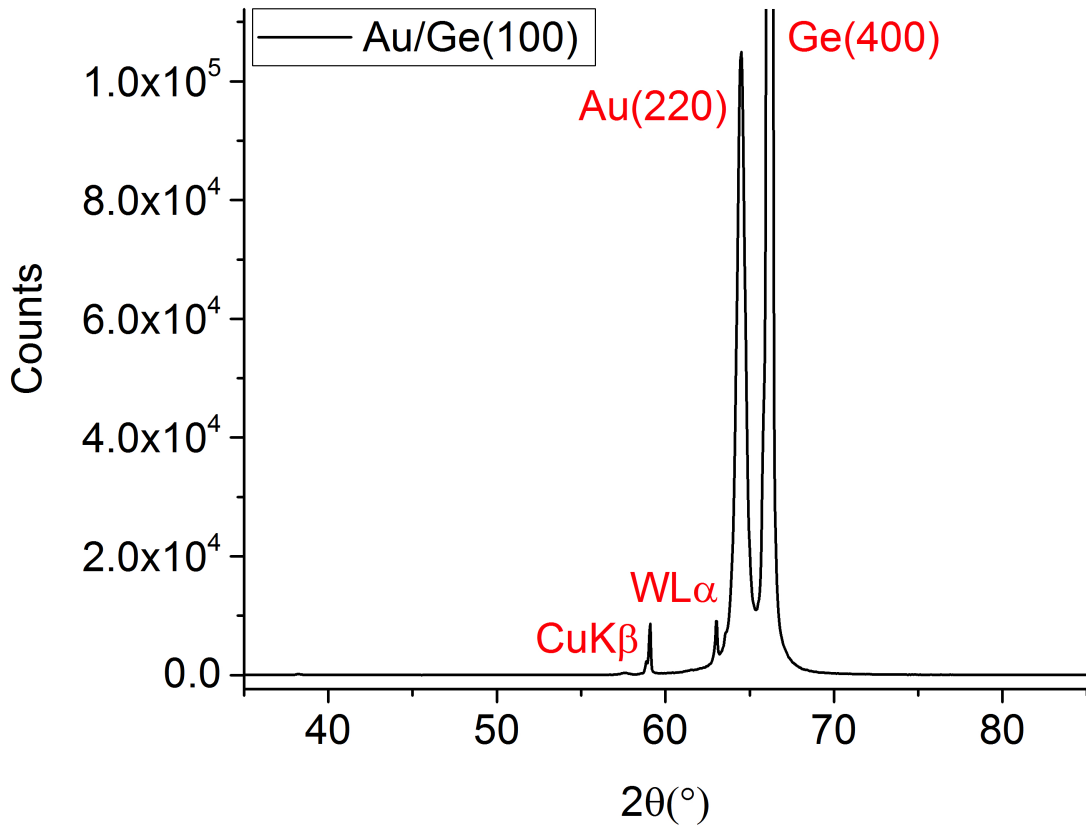

Figure S3: $\theta - 2\theta$ scan in the parallel beam configuration of Au on Ge(100). The dominant peak is the Au(220) at 64.5°.
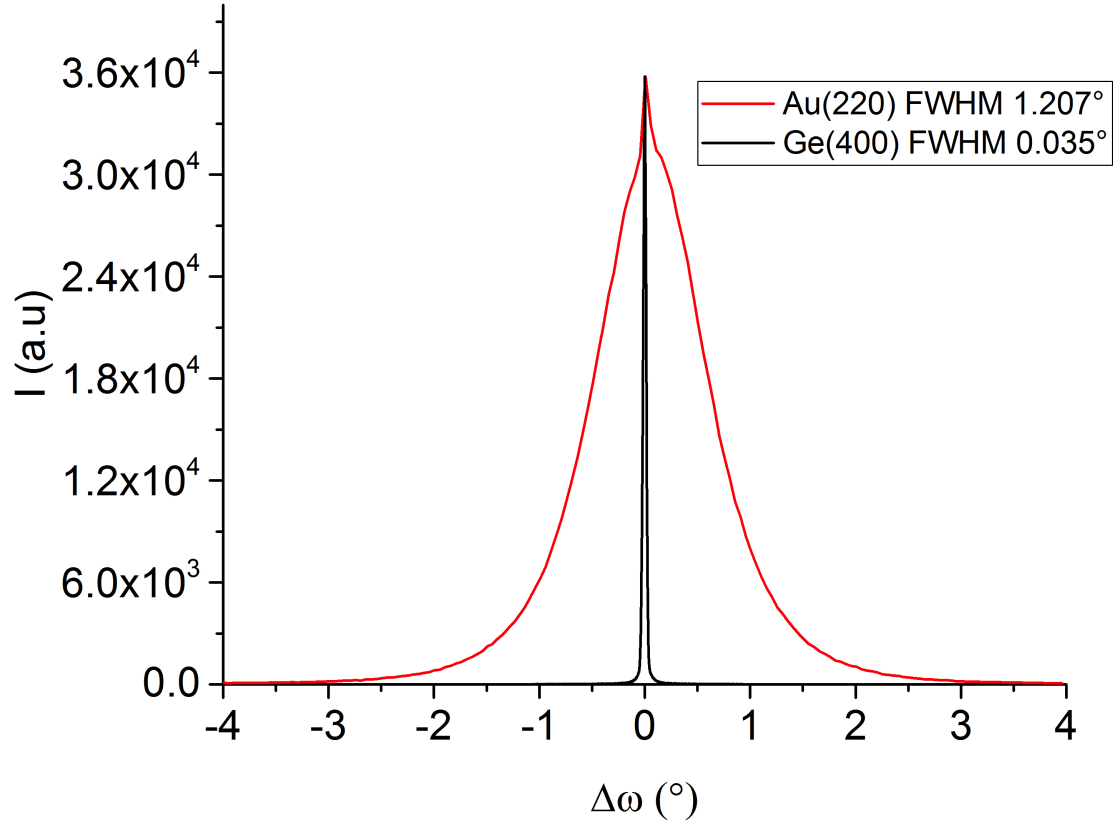
Figure S4: Rocking curves for the Au(220) peak (FWHM = 1.207°) and Ge(400) peak (FWHM = 0.035°).

[110] allows to have three different families of Au planes orthogonal to the Ge substrate, corresponding to the (111), (220) and (200) planes. By performing an XRD ϕ-scans analysis (in the in-plane geometry and in the Bragg conditions for the three families) it is possible to obtain indications about the orientation of the crystalline domains with respect to the Ge substrate. The XRD ϕ-scans patterns were plotted after an angular correction (each pattern was shifted to the left by an angle equal to the Bragg angle θ_B, Figure S5). Under these conditions it was possible to see which planes are parallel (aligned peaks) and determine the angle between a family of planes of Au and of Ge(100). In particular each one of the Au(220) and Au(200) planes shows four peaks in the ϕ-scans, shifted by 45° with respect to the Ge(100) substrate. Differently, the plane Au(111) has two, non-equivalent directions
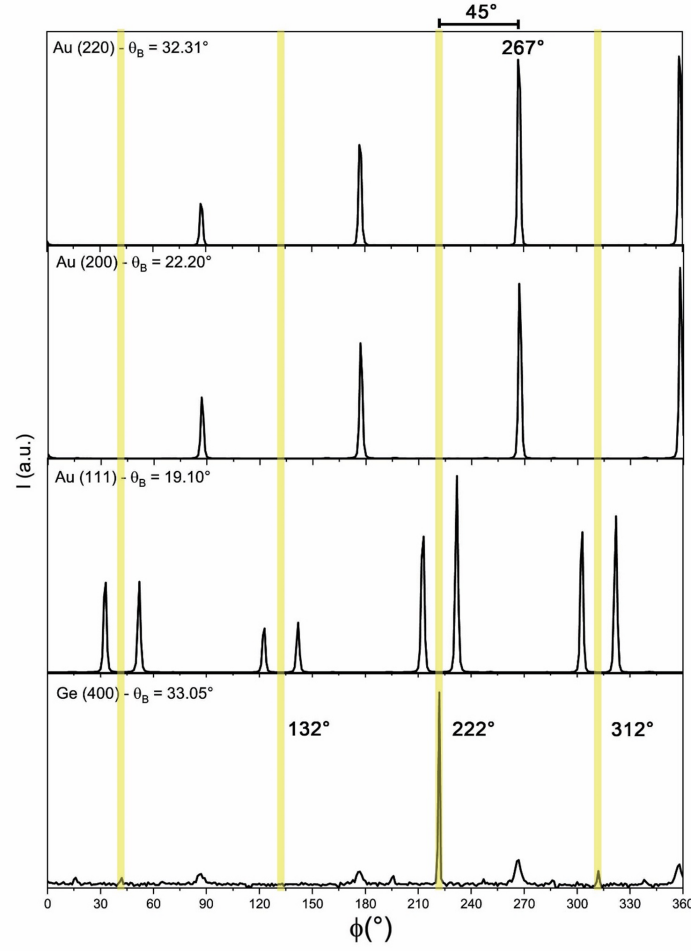
Figure S5: XRD ϕ-scans patterns for the Ge(400), Au(111), Au(200) and Au(220) peaks were plotted after an angular correction (each pattern was shifted to the left by an angle equal to the Bragg angle θ_B).

and shows two series of four peaks shifted by 19° corresponding to the angle formed between the homonymous planes in the two configurations rotated by 90°, cf. Figure S5.

The description of the interface structure obtained using the analysis of the ϕ-scans obtained by XRD provides useful inspiration for theoretical models proposed in the present work; it proves the existence of two preferential absorption sites, which is the key feature of our theoretical models. thus, the small mismatch in the two lattices can be relaxed via the reticular relaxation.
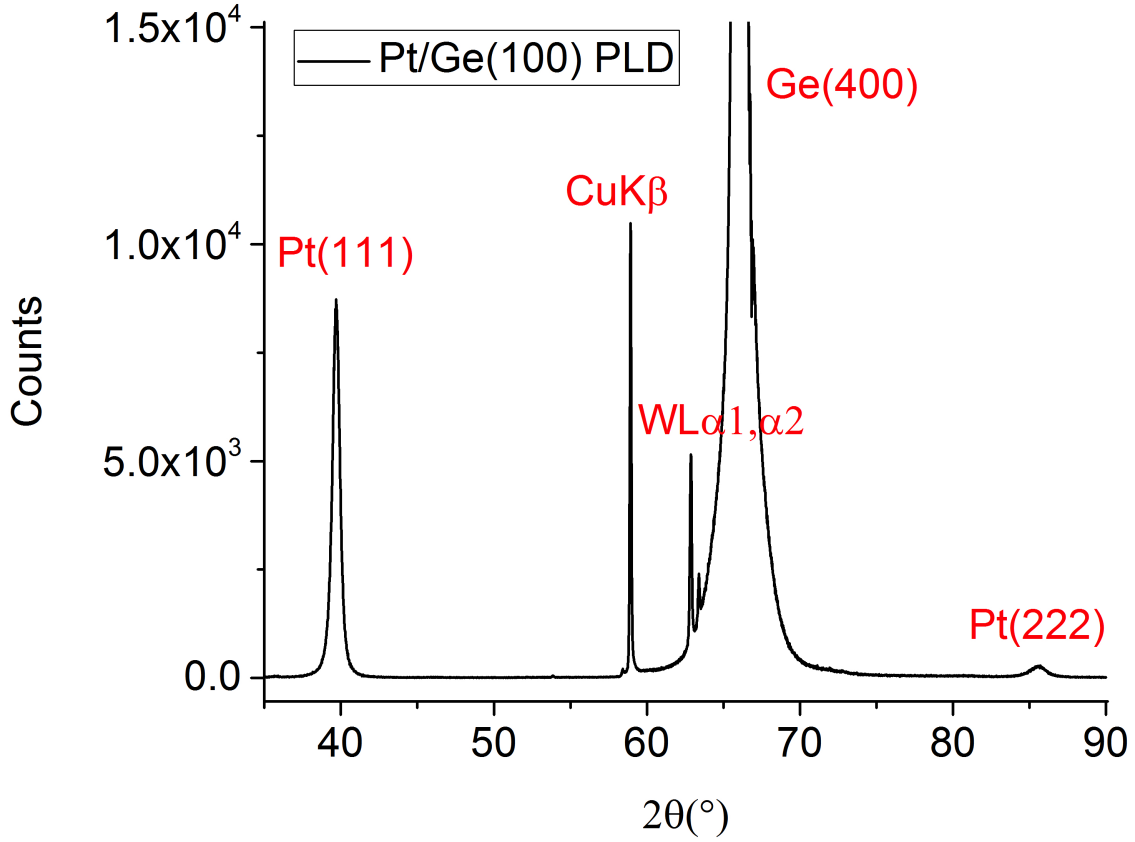
Figure S6: $\theta - 2\theta$ scan in the parallel beam configuration of Pt on Ge(100). The dominant peak is the Pt(111) at 39.69°.

S2.2   Pt/Ge(001) thin films grown by PLD

Interesting differences can be found in the growth of Pt/Ge(100). In this case, the XRD pattern indicates that only the Pt(111) peak at 39.69° is visible (see Figure S6) in good agreement with results from other groups (see for example S. Gaudet et al., J. of Vac. Sci. and Technol. A 24, 474 (2006)). We also observed the CuKβ at 58.9°, the WLα1 at 62.9° and WLα2 at 63.4°. Hence the (111) plane grows with no epitaxial relationship with the substrate and shows polycrystalline texture.
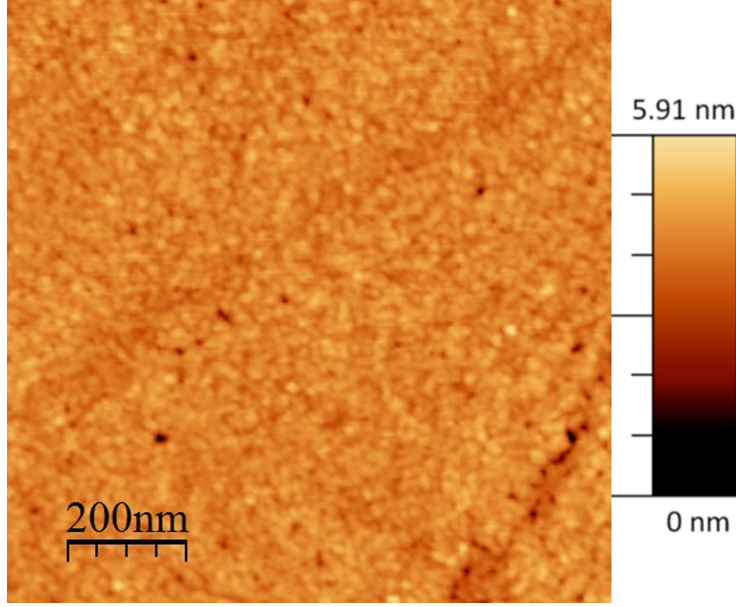
Figure S7: AFM image acquired on Ge(100) after the cleaning procedure described in the main text. Scan size 1000 nm x 1000 nm. Surface roughness 0.33 nm RMS.

S3   AFM Characterization

AFM topographies acquired in tapping mode (Figure S7) after the Ge surface treatment described in the main text indicate a surface roughness of 0.33 nm RMS over areas of 1 μm × 1 μm. This value is in good agreement with that reported by the manufacturer for the pristine wafers, i.e. below 0.5 nm RMS. Hence, an atomically smooth surface morphology is preserved after the wet chemical etching.

S4   Ohmic contact (Al/Ge(100)/Al) characterization

In order to test the quality of the Ohmic contact at low temperature (80 K), we have prepared the junction in the same way as we have prepared the diodes with Au and Pt contact. In this case, instead of the rectifying contact we deposited on the surface of the Ge (100) by PLD an Al film (thickness of about 50 nm). We measured the electrical characteristic (I-V) in these conditions. As it can be seen from Figure 10, the contact is not perfectly Ohmic for the explored polarization bias but, the resistance values of the overall heterostructure
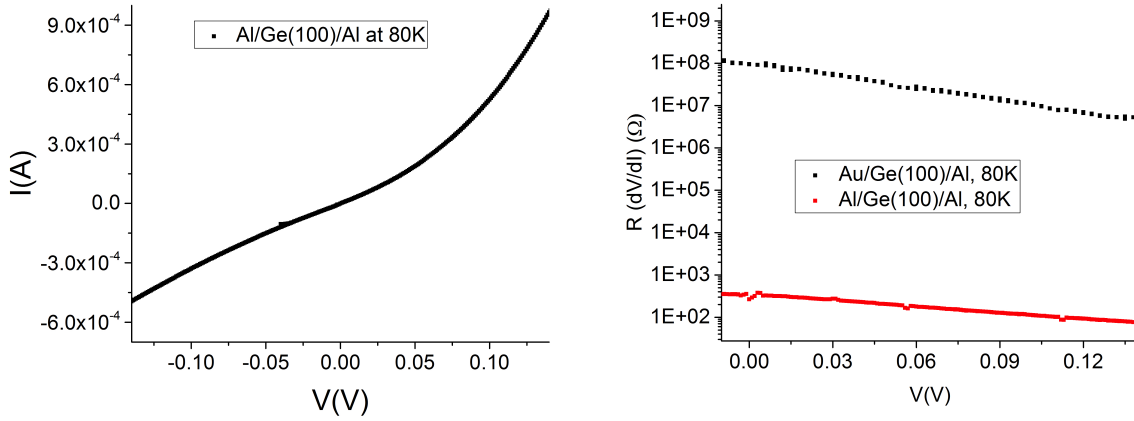
Figure S8: Left panel: current voltage curve of the Al/Ge(100)/Al heterostructure (back-contact). Right panel: comparison of the differential resistance with the Schottky diode Au/Ge(100)/Al at 80K, as a function of bias applied to the junction (right panel).

are in the range of (80-250) Ω. This is not a problem for BEEM measurements since this technique yields a correct measurement of the barrier provided that the resistance of the rectifying junction is higher than the back-contact resistance, which in our case is in the range (5-100) MΩ. In addition, the low temperature BEEM modeling (following the appropriate correction of the thermal effects) allows an accurate estimate of the barrier without requiring the modeling of parallel transport mechanisms. Finally, the measurement takes place at zero bias (not polarized junction), which constitutes a further advantage for the BEEM measurement.

S5   I-V vs T characterization

It is well known that the behavior of the Schottky junctions at low temperature is much more complex and frequently the phenomenological models fail. In particular in our case the net doping concentration is 3.4 to 4.0 10^{14} cm^{-3} with a depletion length of about 1 μm. Given such a large depletion width, the emergence of TFE is not expected at low temperature, rather TE might be assumed to dominate transport. Indeed, the characteristic energy E_{00}[13] results to be $\ll 1$ in our case, which confirms previous arguments. Interpolation of the I-V

curves with TE model down to 55 K however indicates a strongly non-ideal behavior of the macroscopic transport at low T. This is embodied by the fact that both the SBH and the ideality index greatly vary with T and achieve non-realistic values (SBH ≈ 0.15 eV, $n \approx 8$) at 50 K. This is a well-known behavior reported in literature for several Schottky junctions and it very likely reflects failure of the simple TE theory due to additional complexity of interfacial transport, e.g. originated by spatial inhomogeneity, bias voltage dependence of the barrier height, image-force lowering or even interface states. The BEEM, being a microscopic technique, it cannot map the whole junction extensively but can give information about interfacial band bending over a limited portion of the interface (compared to the whole ≈ 2 mm^2 macroscopic area of the Schottky barrier diode). Hence, we cannot exclude that a few, small regions of the interface - that have not been directly studied by BEEM - might in turn have an important effect on the temperature evolution of the studied interfaces. In this respect we recall that the previous discussion and data of Figure S9 indicate that extraction of the SBH as a function of T from macroscopic I-V-T data is not straightforward for the prepared Au/Ge(100) and Pt/Ge(100). On the contrary, BEEM allows an easier modeling of the interface barrier (after thermal correction) without the polarization of the junction even if in this case the cooling of the device has become necessary since at room temperature the ballistics signal is covered by the thermal noise of the junction. At room temperature, only barriers higher than 0.7 eV can be measured.[14]

S6 Theoretical Modelling of Interfaces

Due to the lack of detailed experimental information on the atomistic geometry of the interface we resort to models obtained by optimizing geometries derived from a plane-waves DFT formalism for stacks of metallic layers deposited on Ge{001}.[15,16] This is necessary because detailed atomic positions are a required input to ab-initio calculations for BEES spectra which, in turn, provide the required effective phase-space volume determined by μ.
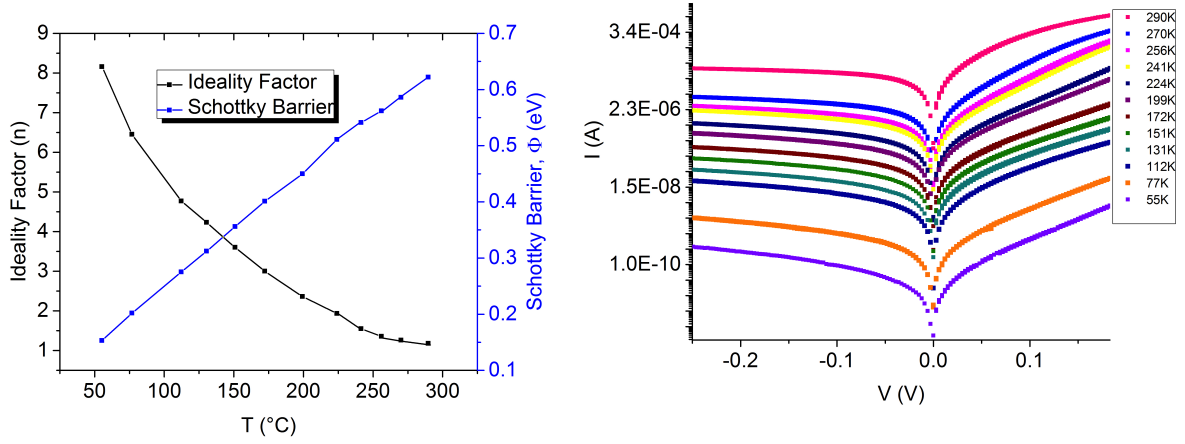
Figure S9: Current voltage macroscopic characterization as function of temperature (left panel). Ideality factor m, and Schottky barrier Φ, calculated fitting the experimental data using the TE model (right panel).
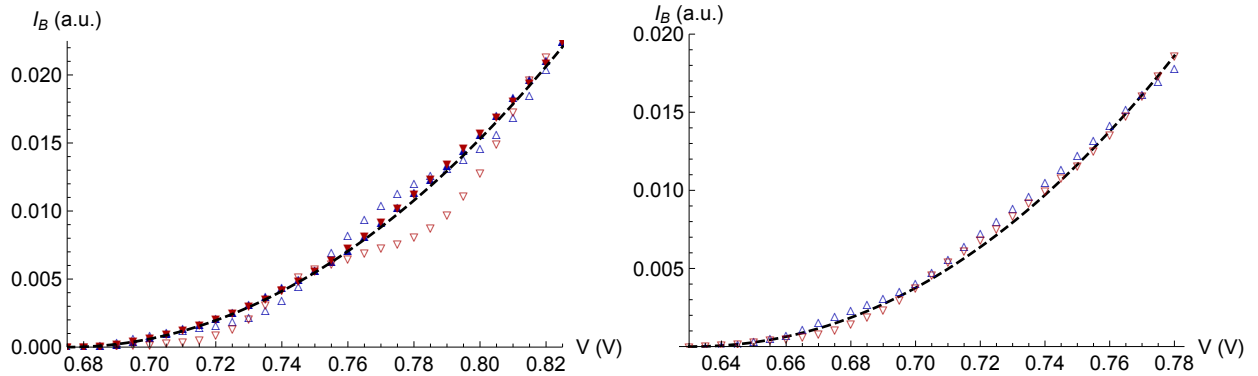

Figure S10: Best fit determination of μ from ab-initio IV. Left panel: $\sqrt{2} \times \sqrt{2}$ R45° Pt(001)/1 × 1 Ge(001); registry BB is given in blue (filled up-triangles 16384 special points, empty up-triangles 9216 special points) and TH is given in red (same notation, down-triangles). Black dashed line is a $V^{2.01}$ best fit to ab-initio theory values. Right panel: idem for 1 × 7 Au(011)/ 1 × 5 Ge(001), 4096 special points. Black dashed line is a $V^{2.11}$ best fit to ab-initio theory values. For the sake of clarity in the presentation both registries have been displaced to a common origin and have been scaled to coincide at the end of the interval, $V = \Phi + 0.15$ eV.

S6.1   Ab-initio determination of μ

Regardless of the orientation of metalic planes forming the interface with Ge(001), ab-initio BEEM IV curves given by Equation Equation **??** can be fitted well by an effective phase-space model as proposed in Equation **??**. Power-law fitting in the interval $(\Phi, \Phi + \Delta)$ yields a consistent picture for the value of μ, provided that the interval is large enough to include the second threshold determined from experimental data, $\Delta \geq 0.11$, but short enough to exclude the first secondary minimum in Ge electronic bandstructure, $\Delta \leq 0.15$. Finally, it is important to use a small enough value of $\eta \leq 0.005$ eV and, a dense enough special points mesh in the 2D interfacial Brillouin zone to avoid spurious oscillations related to the internal precision of calculations. Figure S10 shows the quality of the effective phase-space
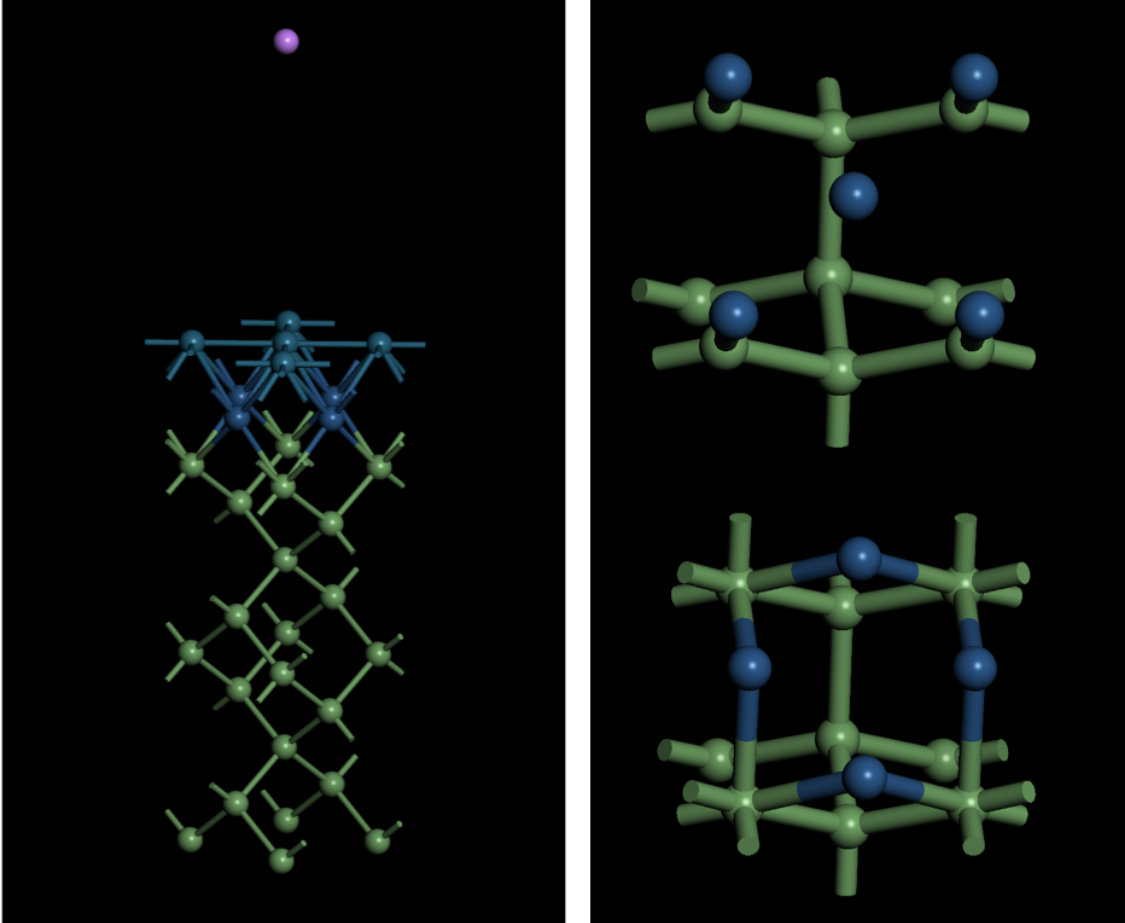

Figure S11: Schematic representation for the interface $\sqrt{2} \times \sqrt{2}$ R45° M(001) / 1×1 Ge(001). Tip (violet), Metal (blue), Semiconductor (green). The two panels on the right show the highly symmetric configurations: bridge-bridge (BB, bottom) and atop-hollow (TH, top).
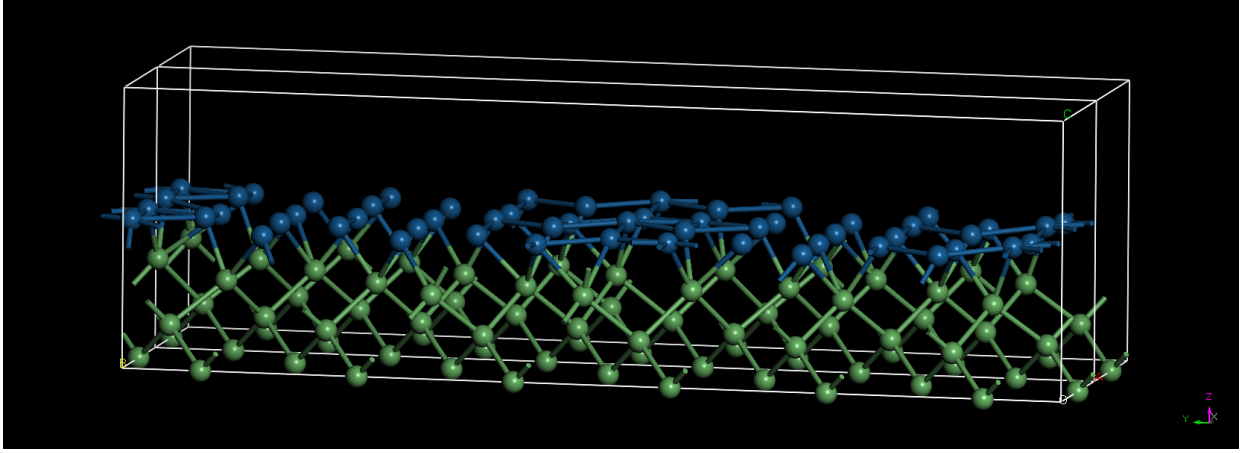
Figure S12: Optimized model interface for 2×7 Pt(111) / 1×6 R45° Ge(001) (top and side views). Notice the significant amount of disorder on the layer of platinum, making difficult the formation of a good epitaxy.

Table S1: Summary of results for interfacial atomistic models. ΔE (eV) gives the difference in the total energy between two registries. σ_{xx} and σ_{yy} (MPa) are residual stresses in the interfacial 2D unit cell. $< d_{Ge-M} >$ is the average distance between atomic planes accross the metal/semiconductor interface and, Δd_{M_1} is the maximum corrugation in the last metalic layer. Q_{Ge} and Q_M are the average unbalanced electronic charge on the Ge/M atomic planes across the interface (in units of the electron charge).

	ΔE	σ_{xx}	σ_{yy}	$< d_{Ge-M} >$	Δd_{M_1}	Q_{Ge}	Q_M
	$\sqrt{2} \times \sqrt{2}$ R45° M(001) / Ge(001)						
Au (BB)	0.0	−0.6	−1.1	2.1	0.5	+0.5	−0.2
Au (TH)	0.5	−0.4	−0.7	2.5	0.1	+0.5	−0.4
Pt (BB)	0.0	+1.2	+1.0	1.7	0.2	+0.6	−0.2
Pt (TH)	1.1	+1.8	+1.5	2.3	0.1	+0.5	−0.3
	1×7 Au(011) / 1×5 Ge(001)						
Au (B)	1.1	−0.9	−0.3	1.7	0.4	+0.7	−0.2
Au (T)	0.0	−1.2	−0.4	2.1	0.5	+0.8	−0.2
	2×7 Pt(111) / 1×6 R45° Ge(001)						
Pt	0.0	+3.6	+3.2	1.9	0.4	+0.7	−0.2

ballistic model representing the full ab-initio calculation in a small region near the onset. For $\sqrt{2} \times \sqrt{2}$ R45°-Pt(001) we find that 16384 special points already yield enough precision (left panel, filled triangles), where we remark how half that number was not enough to reach good convengence and oscillations around the power law can still be seen (emptied triangles). Notice the similarity between both registries, provided they are displaced to share the same
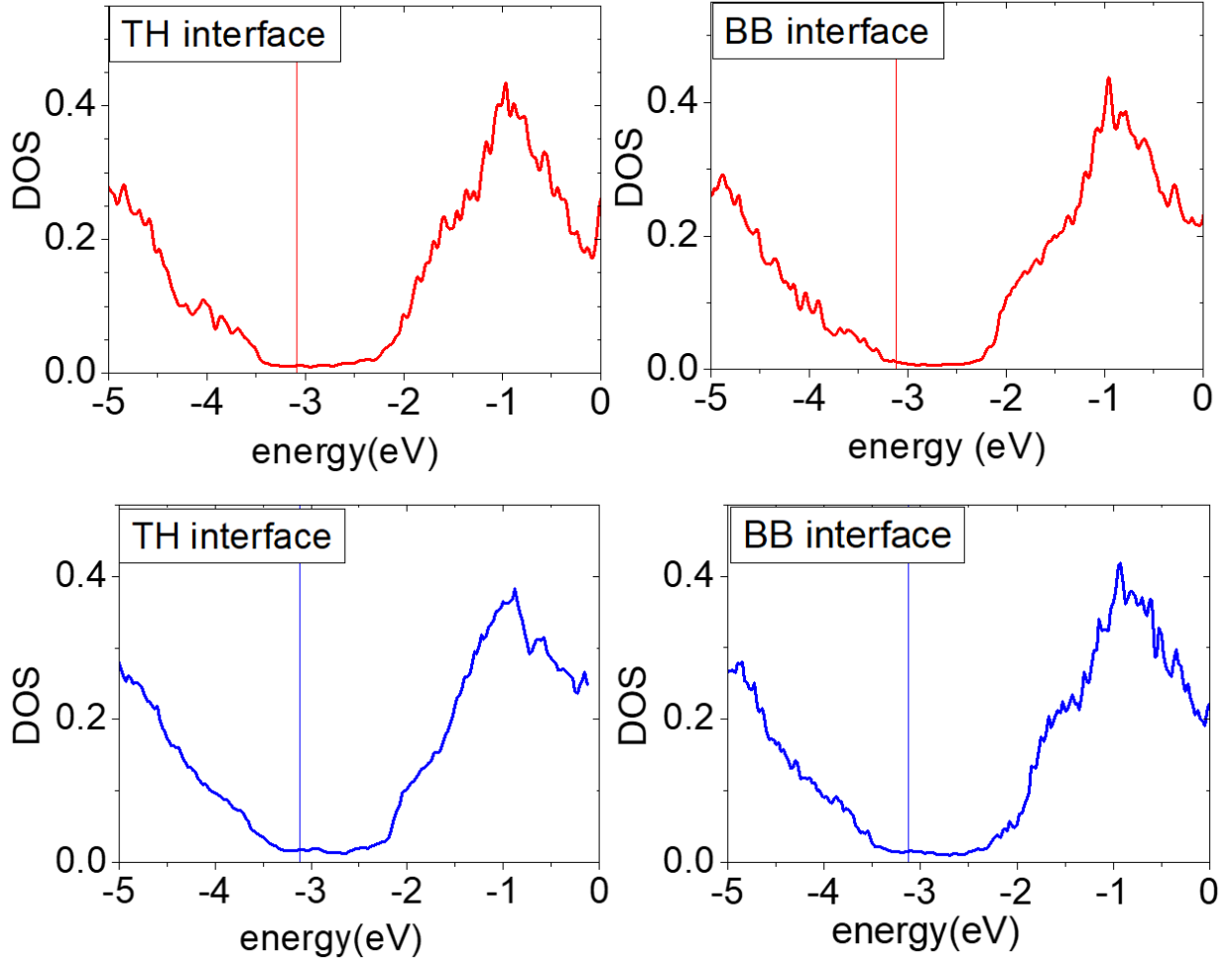
Figure S13: Theoretical calculation of the Density of States for Au/Ge (top) and Pt/Ge (bottom). The Fermi level (vertical lines) shift w.r.t the valence band by 0.1 and 0.05 eV, respectively.

value for the onset. The right panel of Figure S10 shows similar results for 1×7 Au(011)/ 1×7 Ge(001). We conclude that fits of ab-initio data to a power law are excellent under the right conditions and, they may be taken as independent of the metalic face orientation and the registry.

S6.2   Atomic Configurations for M/Ge(001) Interfaces

For the Au/Ge(001) interface, STM structural work has identified major domains for metal growth along planes Au(011), Au(111) and Au(001).[17,18] Therefore, we have analyzed the-

oretical models where we optimize atomic arrangements at the interface by stacking layers with these three orientations. Au and Pt are face cubic centered metals with a similar lattice parameter, 4.065 Å and 3.912 Å. To match the 1×1 2D square unit cell of Ge(001) defined by perpendicular vectors $\mid \vec{v}_1 \mid = \mid \vec{v}_1 \mid = 4.001$ Å we consider the following arrangements $\sqrt{2} \times \sqrt{2}$ R45° M(001) / 1×1 Ge(001), 1×7 M(011) / 1×5 Ge(001) and, 2×7 M (111) / 1×6 R45° Ge(001), hereafter M(001), M(011) and M(111) for the sake of brevity. All these configurations yield small interfacial stress for the smallest possible size of the 2D cell.

For these calculations we have used plane-waves DFT as implemented in CASTEP,[19] Perdew-Burke-Ernzerhof GGA-XC,[20] and a sampling of the Brillouin zone with $\Delta k = 0.04$ Å^{-1}. Stacking of M(001) planes were optimized with on-the-fly norm-conserving pseudopotentials and a 1200 eV energy cutoff, while for M(011) and M(111) on-the-fly soft pseudopotentials and a 400 eV energy cutoff were used, due to the large amount of atoms involved. Threshold values for convergence were 10^{-6} eV for the total energy after each optimization cycle, a maximum force of 0.01 eV/A, and a maximum displacement of any atom of 5×10^{-4} Å.

M(001) layers allow for the simplest interfacial model by a simple 45° rotation. Two symmetry sites related by a $\frac{1}{2}(\vec{v}_1 + \vec{v}_2)$ shift become reasonable candidates for a minimum total energy interface. In one case both metal atoms adsorb on the two bridges of the Ge(001) cell, hence labelled BB, while in the other case one atom sits on atop and the other on hollow (labelled TH), cf. Figure S11. For Au, BB is preferred over TH by -0.5 eV per unit cell, while for Pt BB is preferred by -1.1 eV i.e. 0.001% (Au) and 0.003% (Pt) w.r.t the total energy. Residual stresses are very similar in both cases, in the order of $\sigma_{xx} \approx \sigma_{yy} \approx 1$ MPa, cf. Table S1. In all cases, the last Ge layer tends to be positively charged, while the first M layer attracts extra negative charge.

M(011) layers also allow for two symmetry-related registries which are similar in total energy. In the preferred configuration, the metalic atom adsorbs near atop and quasi-bridges (T), cf. Figure 4 in the main text (left panel), while in the next configuration metalic atoms

adsorb near bridges (T). Corresponding parameters for these two geometries take values quite similar as the M(001) case, cf. Table S1.

Finally, M(111) can be formed on the Ge(001) surface in such a way that all important symmetry sites, i.e. atop, bridge and hollow, are more or less equally occupied, cf. Figure S12. There seems not to be an obvious registry shift by mixing the four-fold rotational axis for the substrate and the three-fold one that corresponds to the metalic layer. On the other hand, this model results in residual stresses about twice the typical values found for (001) and (011) orientations. Therefore, we expect to find more defects, like domain walls and vacancies, associated to these layers. Which is, in fact, compatible with our experimental observations by XRD, cf. Section S2.2.

The calculated structures have been transferred to the localized-basis ab-initio DFT, FIREBALL in order to obtain the hamiltonian required by the BEES formalism.[21] For this calculation, we have included additional bulk-like layers in the interface. All the interfaces were created with 12 layers on the metallic part and 16 in the semiconductor side (saturated by H atoms at the backside). Charges have been converged using 4096, 256 and 64 k-points to sample the Brillouin zone for the (001), (011) and (111) metallic orientations, respectively.

S6.3   Schottky Barrier and Interface Dipole

Figure S13 shows the density of states at the $\sqrt{2} \times \sqrt{2}$ R45° Au(001) / Ge(001) interface for the two registries: BB and TH. The diferent position of the Fermi Level at the interface with respect to the conduction band of the semiconducting bulk explains the appearance of different barriers associated to each structure. The interfacial dipole has been computed by comparing the shift in the Fermi level with respect to the valence band edge for bulk Ge and the metal-semiconductor interface plus the shift of Ge low-lying s level between both systems.[22]

For $\sqrt{2} \times \sqrt{2}$ R45° Au(001) / Ge(001) we find $\Delta_{Au(001)} = 0.1$ eV, while for 1×7 Au(011) / 1×5 Ge(001) is $\Delta_{Au(011)} = 0.07$ eV, both in good agreement with our experimental findings.

Finally, for $\sqrt{2} \times \sqrt{2}$ R45° Pt(001) / Ge(001) we obtain $\Delta_{Pt(001)} = 0.05$ eV, a little bit short of the value 0.11 eV derived from the fit, but still in good agreement with the experiment after taking into account the complexity of the actual interface.

References

(1) Moulder, J.; Stickle, W.; Sobol, P.; Bomben, K. *Handbook of X-ray Photoelectron Spectroscopy*; Perkin-Elmer Corp, Eden Prairie, MN, 1992.

(2) Barr, T. L.; Seal, S. Nature of the use of Adventitious Carbon as a Binding Energy Standard. *J. Vac. Sci. Technol. A* **1995**, *13*, 1239–1246.

(3) Greczynski, G.; Hultman, L. C 1s Peak of Adventitious Carbon Aligns to the Vacuum Level: Dire Consequences for Material's Bonding Assignment by Photoelectron Spectroscopy. *ChemPhysChem* **2017**, *18*, 1507–1512.

(4) NIST X-ray Photoelectron Spectroscopy Database, v4.1. National Institute of Standards and Technology, Gaithersburg, 2012; http://srdata.nist.gov/xps/.

(5) Sun, S.; Sun, Y.; Liu, Z.; Lee, D.-I.; Peterson, S.; Pianetta, P. Surface Termination and Roughness of Ge(100) cleaned by HF and HCl solutions. *App. Phys. Lett.* **2006**, *88*, 021903.

(6) Rivillon, S.; Chabal, Y. J.; Amy, F.; Kahn, A. Hydrogen Passivation of Germanium (100) Surface using Wet Chemical preparation. *App. Phys. Lett.* **2005**, *87*, 253101.

(7) Deegan, T.; Hughes, G. An X-ray Photoelectron Spectroscopy study of the HF Etching of Native Oxides on Ge(111) and Ge(100) Surfaces. *Appl. Surf. Sci.* **1998**, *123-124*, 66 – 70.

(8) Park, K.; Lee, Y.; Lee, J.; Lim, S. Oxidation Mechanism of Hydrogen-Terminated Ge(100) Surface. *Appl. Surf. Sci.* **2008**, *254*, 4828 – 4832.

(9) Hu, J.; Wong, H.-S. P.; Saraswat, K. Novel Contact Structures for High Mobility Channel Materials. *MRS Bull.* **2011**, *36*, 112–120.

(10) Bobisch, C. A.; Bannani, A.; Koroteev, Y. M.; Bihlmayer, G.; Chulkov, E. V.; Möller, R. Conservation of the Lateral Electron Momentum at a Metal-Semiconductor Interface Studied by Ballistic Electron Emission Microscopy. *Phys. Rev. Lett.* **2009**, *102*, 136807.

(11) Bannani, A.; Bobisch, C. A.; Matena, M.; Möller, R. Ballistic Electron Emission Spectroscopy on Ag/Si Devices. *Nanotechnology* **2008**, *19*, 375706.

(12) Ventrice, C.; LaBella, V.; Ramaswamy, G.; Yu, H.-P.; Schowalter, L. Hot-Electron Scattering at AuSi(100) Schottky Interfaces measured by Temperature dependent Ballistic Electron Emission Microscopy. *Appl. Surf. Sci.* **1996**, *104-105*, 274 – 281, Proceedings of the Fifth International Conference on the Formation of Semiconductor Interfaces.

(13) Padovani, F.; Stratton, R. Field and Thermionic-Field Emission in Schottky Barriers. *Solid-State Electron.* **1966**, *9*, 695 – 707.

(14) Prietsch, M. Ballistic-Electron Emission Microscopy (BEEM): Studies of Metal/Semiconductor Interfaces with Nanometer Resolution. *Phys. Rep.* **1995**, *253*, 163 – 233.

(15) Hohenberg, P.; Kohn, W. Inhomogeneous Electron Gas. *Phys. Rev.* **1964**, *136*, B864–B871.

(16) Kohn, W.; Sham, L. J. Self-Consistent Equations Including Exchange and Correlation Effects. *Phys. Rev.* **1965**, *140*, A1133–A1138.

(17) Wang, J.; Li, M.; Altman, E. Scanning Tunneling Microscopy study of Au Growth on Ge(001): Bulk Migration, Self-organization, and Clustering. *Surf. Sci.* **2005**, *596*, 126 – 143.

(18) Jany, B. R.; Gauquelin, N.; Willhammar, T.; Nikiel, M.; van den Bos, K. H. W.; Janas, A.; Szajna, K.; Verbeeck, J.; Aert, S. V.; Tendeloo, G. V.; Krok, F. Controlled

Growth of Hexagonal Gold Nanostructures during Thermally Induced Self-assembling on Ge(001) Surface. *Sci. Rep.* **2017**, *7*, 42420.

(19) Clark, S. J.; Segall, M. D.; Pickard, C. J.; Hasnip, P. J.; Probert, M. I. J.; Refson, K.; Payne, M. C. First-Principles Methods using CASTEP. *Z. Kristallogr.* **2005**, *220*, 567–570.

(20) Perdew, J. P.; Burke, K.; Ernzerhof, M. Generalized Gradient Approximation Made Simple. *Phys. Rev. Lett.* **1996**, *77*, 3865–3868.

(21) Lewis, J.; Jelinek, P.; Ortega, J.; Demkov, A. A.; Trabada, D. G.; Haycock, B.; Wang, H.; Adams, G.; Tomfohr, J. K.; Abad, E.; Wang, H.; Drabold, D. A. Advances and Applications in the FIREBALL *ab-initio* Tight-Binding Molecular-Dynamics Formalism. *Phys. Status Solidi B* **2011**, *248*, 1989–2007.

(22) Flores, F.; Tejedor, C. On the Formation of Semiconductor Interfaces. *J. Phys. C: Solid State Phys.* **1987**, *20*, 145–175.